JGR Space Physics

RESEARCH ARTICLE
10.1029/2019JA027057

Quantification of the Vertical Transport and Escape of Atomic Hydrogen in the Terrestrial Upper Atmosphere

P. P. Joshi[1], **Y. D. Phal**[1], **and L. S. Waldrop**[1]

[1]Department of Electrical and Computer Engineering, University of Illinois at Urbana-Champaign, Urbana, IL, USA

Key Points:

- Radiative transfer inversion of Ly_α emission measured by TIMED/GUVI is used for estimation of vertical H flux and density from 250 km to 1 RE
- Total terrestrial H escape is observed to be diffusion-limited at a nearly constant rate of $\sim 1.2 \times 10^8$ atoms $cm^{-2}s^{-1}$ over the solar cycle.
- Jeans' thermal escape comprises up to ~84% of the total flux during solar maximum, whereas non-thermal processes dominate in solar minimum.

Correspondence to:
P. P. Joshi,
ppjoshi2@illinois.edu

Citation:
Joshi, P. P., Phal, Y. D., & Waldrop, L. S. (2019). Quantification of the vertical transport and escape of atomic hydrogen in the terrestrial upper atmosphere. *Journal of Geophysical Research: Space Physics*, *124*, 10,468–10,481. https://doi.org/10.1029/2019JA027057

Received 24 JUN 2019
Accepted 6 AUG 2019
Accepted article online 30 OCT 2019
Published online 09DEC 2019

Abstract Measurements of the limiting escape rate of atomic hydrogen (H) atoms at Earth and the relative significance of thermal evaporation and nonthermal escape mechanisms, such as charge exchange and polar wind, have long been lacking. Our recent development of sophisticated radiative transport analysis techniques now enables the reliable interpretation of remotely sensed measurements of optically thick H emission, such as those acquired along the Earth's limb by the Global Ultraviolet Imager (GUVI) onboard the NASA Thermosphere Ionosphere Mesosphere Energetics and Dynamics (TIMED) spacecraft, in terms of physical parameters such as exobase density and, crucially, vertical diffusive flux. In this work, we present results from a systematic investigation of H Ly_a emission measured by TIMED/GUVI along the Earth's dayside limb from 2002–2007, which we use to derive the vertical H flux and associated density distribution from 250 km out to 1 Earth radius. Our analysis reveals that the vertical flux of thermospheric H is nearly constant over a large range of solar activity and typically exceeds the calculated thermal evaporative flux, suggesting that terrestrial H escape is indeed limited by its vertical diffusion. The excess supply of H atoms to the exobase associated with large observed vertical fluxes requires that nonthermal escape mechanisms be operative for steady-state continuity balance. We find that such nonthermal processes are a particularly significant component of total H escape during low solar activity, when thermal evaporation is weakest.

1. Introduction

Atomic hydrogen, H, is the lightest neutral species in the terrestrial atmosphere, which originates in the mesosphere/lower thermosphere (MLT), becomes increasingly important at higher altitudes in terms of relative abundance, and eventually dominates exospheric composition above 1,000 km in a diffuse cloud known as the geocorona (Chamberlain, 1963). Classical theory views thermal evaporation (Jeans' escape) as the dominant driver of exospheric structure as well as permanent H escape to interplanetary space, whereby most atoms follow ballistic trajectories and only a fraction of H atoms in the high-energy tail of its quasi-Maxwellian velocity distribution attain the necessary escape velocity (Jeans, 1923). However, this theory is incomplete at Earth, since charge exchange reactions between exospheric H atoms and ambient ions energetically and dynamically couple the upper atmosphere with the ionosphere, plasmasphere, and magnetosphere (Banks & Kockarts, 1973; Krall et al., 2018).

Ion-neutral coupling between exospheric H and plasmaspheric H^+, first proposed as a mechanism for enhanced H escape by Cole (1966) and Tinsley (1973); see Hodges (1994), for a thorough review of the literature), effectively replaces a cold (thermal) H atom with a hot one, which then more easily escapes Earth's gravity. The nearly resonant charge exchange between ionospheric H^+ and thermospheric O atoms also generates a kinetically energized H population, albeit at lower effective temperatures due to reduced ion energies at these altitudes (Shizgal & Lindenfeld, 1982). Meanwhile, near the geomagnetic poles, charge exchange reactions between H and O^+ ions further enhance atmospheric H loss, since the resulting H^+ ions are readily accelerated upward as polar wind and escape along the open, nearly vertical geomagnetic field lines via ambipolar diffusion (Banks & Holzer, 1968; Ganguli, 1996; Glocer et al., 2007, 2009, 2012). Exospheric structure is expected to exhibit spatial asymmetries associated with these processes, such as polar depletions and enhanced densities near the magnetic equator (Hodges, 1994; Thomas & Vidal-Madjar, 1978; Tinsley et al., 1975; Vidal-Madjar & Bertaux, 1972; Vidal-Madjar & Thomas, 1978). However, to date,

reported observations of the global, three-dimensional, and time-varying terrestrial H density distribution are notoriously sparse and of insufficient accuracy to allow reliable quantification of the partitioning between thermal and nonthermal escape pathways (Carruthers et al., 1976; Cucho-Padin & Waldrop, 2018; Kameda et al., 2017).

Semiempirical evidence for significant nonthermal H escape was first reported more than four decades ago, based on theoretical calculations and observations of the vertical diffusion of H atoms from their MLT source (Hunten & Strobel, 1974; Liu & Donahue, 1974a, 1974b, 1974c), together with kinetic theory calculations of the thermal (Jeans') escape flux from the exobase based on OGO-5 data (Bertaux, 1975). In order to maintain H continuity throughout the coupled thermosphere-exosphere, the vertical diffusive flux constitutes the upper limit (the "limiting flux") governing the total rate of H mass loss, regardless of the pathway (Catling & Kasting, 2017; Colegrove et al., 1966; Hunten, 1973). Observations of ultraviolet H emission by the OGO-5 satellite revealed that the thermal evaporative flux increases substantially with increasing exobase temperature and thus solar activity, despite a corresponding but weaker decrease in exobase H density (Bertaux, 1975). Moreover, Jeans' flux was found to be significantly lower, even at solar maximum, than the estimated vertical limiting flux of $\sim 1.5 \times 10^8$ atoms $cm^{-2}s^{-1}$, suggesting that nonthermal H escape processes must be operative and become increasingly significant with reduced solar activity.

This climatological trend was subsequently confirmed by Monte Carlo simulations of thermosphere and exospheric kinetics that explicitly included $H-H^+$ charge exchange energization and polar wind (Hodges, 1994), as well as by photochemical modeling of H chemistry in the mesosphere and thermosphere (Yung et al., 1989) and semiempirical kinetic theory calculations of charge exchange with H^+ (Shizgal & Lindenfeld, 1982). $H-H^+$ charge transfer collisions were found to constitute the dominant mechanism for H escape at solar minimum, ranging from ~60% of the total (Yung et al., 1989) up to ~90% (Shizgal & Lindenfeld, 1982), and to exhibit decreasing importance with increasing solar activity and thus thermospheric temperature. As expected, Jeans' escape was observed to be weakest at solar minimum, when it contributed only 10% to 25% to the total escape flux (Shizgal & Lindenfeld, 1982; Yung et al., 1989), while polar wind was found to be the least significant pathway, constituting ~7–15% of the total with little solar activity variability (Hodges, 1994).

Comprehensive empirical confirmation of the value of the limiting escape flux, its partitioning among thermal and nonthermal pathways, and their predicted climatological trends has long been lacking. Estimates of the limiting H flux range from 1.5×10^8 atoms $cm^{-2}s^{-1}$ to 3.5×10^8 atoms $cm^{-2}s^{-1}$ (Catling & Kasting, 2017; Hunten & Strobel, 1974; Shizgal & Lindenfeld, 1982; Yung et al., 1989). Studies generally suggest that the limiting flux is governed almost entirely by the mixing ratio of the element H (in all chemical forms) near 100 km, such that its dependence on solar activity is weak for exobase temperatures ranging from 750 K to 1350 K (Bertaux, 1975; Hunten & Strobel, 1974; Liu & Donahue, 1974a; Shizgal & Lindenfeld, 1982).

Mesospheric H transport is governed by both eddy and molecular diffusion (Catling & Kasting, 2017), though long standing uncertainties in the eddy diffusion coefficient, k_{zz}, have precluded incorporation of eddy diffusion terms in the calculation of the limiting escape flux. Recently, Swenson et al. (2018) rigorously derived k_{zz} and reported its significant (factor of ~2) semiannual variability, similar to Salinas et al. (2016) but at a lower magnitude than previous reports (Qian et al., 2009, 2013). Accounting for eddy diffusion serves to lower the rate of total H escape with respect to current estimates which neglect eddy diffusion and thus motivate this paper's empirical investigation of H escape in the context of both its diffusion-limited flux and the relative significance of charge exchange in driving nonthermal H loss.

The basis for our investigation is the photometric measurement of ultraviolet H emission at 121.6 nm (Lyman-alpha, "Ly_α"), which is generated by the resonant scattering of solar Ly_α photons. The variation of optically thick H Ly_α emission radiance across the Earth's limb in particular is highly sensitive to the H distribution in altitude from the thermosphere to the lower exosphere (~250 km to 1 R_E) (see Bishop, 1991; Waldrop and Paxton, 2013, or Qin and Waldrop, 2016). Such observations were acquired most recently by the Global Ultraviolet Imager (GUVI) onboard NASA's TIMED mission, which launched in 2001 and obtained routine limb scans of H Ly_α emission until mid-2007. Exospheric parameter retrievals from such data typically involve reconciliation between the observed radiance profile and a forward radiative transfer (RT) model that incorporates a parameterized formulation of the underlying H density distribution

that reflects its diffusive transport, thermal evaporation, and charge exchange interactions with ionospheric, plasmaspheric, and ring current ions (Bishop, 1991, 2001; Chamberlain, 1963; Qin & Waldrop, 2016). Charge exchange interactions are well known to perturb the kinetic distribution function of the H atoms by generating a nonthermal population associated with the higher parent ion energies (Hodges, 1994). A truly rigorous RT model of Ly_α photon scattering would accommodate the Doppler line broadening associated with a nonthermal H population, which is expected to be significant beyond a few Earth radii above the exobase (Hodges, 1994). However, because the resulting H velocity distributions are notoriously unknown, and because such a formulation is regardless computationally prohibitive, existing RT models typically adopt a single-component Maxwellian distribution that reflects the properties of the thermal H population. This unphysical assumption, discussed further in Section 4, renders any H densities derived from data/model reconciliation, including those reported here, biased to an unknowable extent. On the other hand, TIMED/GUVI's preferential sampling of the dayside region near and below the exobase provides strong constraints on both the thermal H density and its vertical diffusive flux through the thermosphere, parameters which in turn can constrain H escape partitioning independently of nonthermal effects.

In this work, we present results from our systematic investigation of H Ly_α limb radiances observed by TIMED/GUVI. We derive both the [H] distribution in altitude and its vertical flux in the thermosphere (from ~250 km to ~500 km) as a function of solar activity over the dayside of Earth at midlatitudes. By using the derived estimates of the vertical H flux as a proxy for the total (limiting) H escape flux and by using classical Jeans theory to derive the thermally evaporating component of that flux, we determine the relative significance of thermal and nonthermal H escape pathways as a function of solar activity. Section 2 describes the GUVI instrument and the methodology used to obtain the Ly_α radiance profiles and associated exospheric parameters. Calculations of the thermal and limiting H flux are presented in Section 3 and discussed in Section 4.

2. Data Acquisition and Analysis Methodology

2.1. Measurements of Ly_α Radiance

NASA's TIMED spacecraft was launched on 7 December 2001 into a near-circular polar orbit at 625 km altitude. With an orbital periodicity of 97.8 min, the TIMED satellite completes approximately 15 orbits per day at an inclination of 74.1° from the equator, and full local time precession of the orbit occurs every 120 days. The GUVI is one of four scientific instruments onboard the TIMED satellite (Christensen et al., 1994). GUVI measures the spectral radiance of Earth's far ultraviolet airglow spectrum using a cross-track scanning spectrograph. The instrument's 11.78° field of view is mapped into 14 spatial pixels along the spacecraft orbital track and 160 spectral bins spanning 115–180 nm. The measured spectrum is binned by an onboard detector processor to yield radiance in five distinct wavelength intervals, including H Ly_α emission at 121.6 nm (Paxton et al., 1999).

Multispectral images spanning the Earth's full disk to the antisunward limb are generated by sweeping the field of view from horizon to horizon perpendicular to the spacecraft motion using a scan mirror. The limb scanning portion of the image is binned into 32 pixels, corresponding to lines of sight (LOSs) having local zenith angles, relative to the spacecraft reference frame, of 99.92–112.22°. The tangent point altitudes of the limb scanning LoSs range from 100–520 km (exact values vary by less than 10 km owing to the Earth's curvature at the location of the tangent point) and span ~2° along the spacecraft track (latitude) and ~4° across the track (longitude), as illustrated in Waldrop and Paxton (2013). Further details regarding the GUVI instrument and its operation is described in Christensen et al. (1994).

2.2. Processing of GUVI Ly_α Limb Scans

The top panel in Figure 1 depicts a single orbit trajectory of the TIMED satellite in geocentric solar ecliptic coordinates, in which the $+x$ axis points toward the Sun, the $+z$ axis points toward ecliptic north, and the $+y$ axis points toward the dusk terminator on the ecliptic plane. Contours of constant solar zenith angle (SZA) and the ecliptic plane are superimposed on the spherical Earth surface, and the arrow depicts the antisunward LOS of a nominal cross-track limb scan by GUVI. Panel (a1) of the figure shows the locations of the LOS tangent points (blue dots) associated with each of the 14 × 32 spatial bins comprising a single representative limb scan acquired near the ecliptic plane. The red circle denotes the approximate location of the center of the scan image, which is used to tag each scan to a single spatial location for analysis as described in Section 2.3.

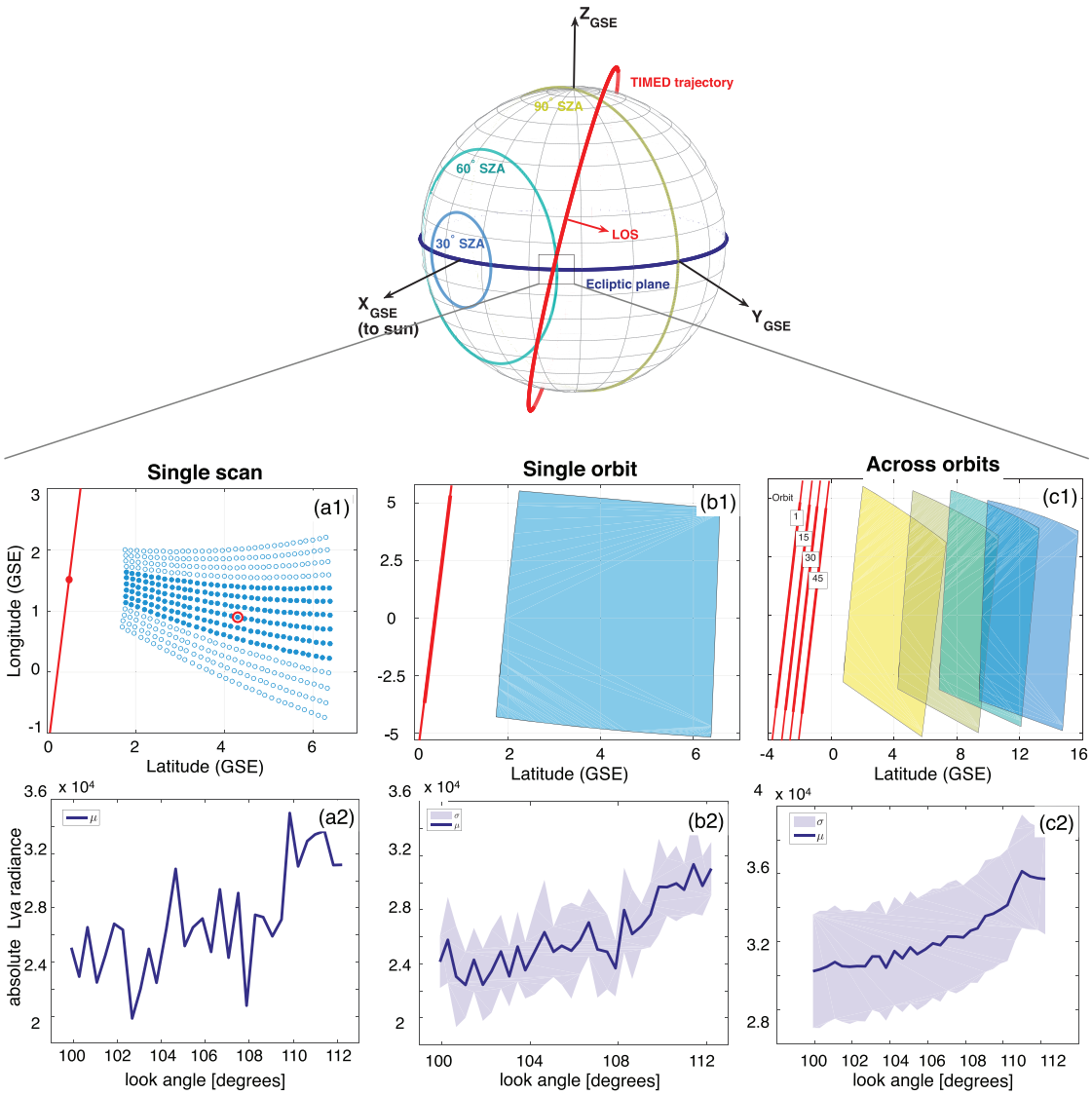

Figure 1. Depiction of TIMED spacecraft single orbital trajectory in GSE coordinates: Contours corresponding to three representative SZAs (30°, 60°, and 90°) are shown. Solid blue line corresponds to the ecliptic plane. (a1) Spatial distribution of tangent points of the 14 × 32 LOSs in a single GUVI limb scan with the six central pixels highlighted. The corresponding limb scan is shown in (a2). (b1) Multiple limb scans from single orbit that are averaged together to yield a radiance profile that is shown in (b2). (c1) Limb scans averaged over three consecutive days. The corresponding 1 × 32 limb scan radiance profile with a distinctive peak at a look angle of 111° is shown in (c2).

GUVI's toroidal diffraction grating causes optical distortions, which manifest as an offset in the SZA of the peak angular response of a pixel at the edge of the slit relative to that at the center. To mitigate this misregistration bias while increasing the signal-to-noise ratio (SNR) of the Ly_α radiance profile across the limb, we begin data processing by averaging each measured 14 × 32 radiance array in the along-track direction among the six central pixels only (see highlighted LOS tangent points in panel (a1)), yielding a single 1 × 32 array of the variation in H Ly_α radiance as a function of local zenith angle of the LOS (the "look angle") from GUVI's instantaneous observing position along the orbit. Panel (a2) in Figure 1 is a representative example of the resulting radiance limb profile.

As the example indicates, single limb scans exhibit significant LOS-to-LOS variability across the profile. This small SNR represents insufficient constraint on RT model inversion (see Section 2.3), such that further averaging is needed for reliable data analysis. Because the RT model is highly sensitive to the incident solar flux, which in turn varies significantly with SZA, such averaging must be performed among scans

acquired at similar SZA values. Defining an SZA bin to span ±5° around the ecliptic plane (i.e., an ecliptic latitude bin) allows for the averaging of ~11–12 consecutive 1 × 32 limb scans along a given orbit into a single "orbit-averaged" 1 × 32 scan, and the resulting viewing geometry is shown in Panel (b1) of Figure 1 as a shaded envelope of LOS tangent points. The corresponding average radiance profile and its standard deviation envelope is depicted in panel (b2).

As a means of further improving the SNR of the scans, we extend the SZA bin for averaging of individual radiance profiles to encompass ±5° SZA along the ecliptic plane (effectively constituting an ecliptic longitude and thus local time bin). TIMED's orbital precession over this range occurs over a span of 3 days, such that more than 500 individual scans spread over ~45 individual orbits are averaged to construct the radiance profiles that we use for RT model inversion and exospheric parameter estimation as described below. Panel (c1) Figure 1 depicts four representative envelopes of orbit-averaged LOS tangent points throughout this interval, while Panel (c2) shows the associated radiance profile. Any scan acquired when Ap>20 is excluded from the average in order to ensure that the reported results correspond to quiet geomagnetic conditions.

2.3. Inverse-Theoretic Estimation of H Density and Escape Flux

H Ly_α emission is generated by the resonant scattering of solar Ly_α photons, and the exosphere is optically thick out to altitudes above Earth's surface of ~2 R_E. As a result, accurate interpretation of measured radiance profiles across the limb requires consideration of both single and multiple scattering of Ly_α photons into and out of the LOS. Our analysis is based on inversion of a forward model of Ly_α RT that was originally developed as the LYAO-RT model by Bishop (2001) and subsequently refined for GUVI analysis as described in Qin and Waldrop (2016). The model features a spherical geometry, incorporates total Ly_α absorption by O_2 below ~80 km, accommodates a nonisothermal temperature profile below the exobase (~466 km), and assumes complete frequency redistribution. The H density below the exobase is parametrized using the analytical formulation described by Bishop (2001) in terms of three free parameters: vertical diffusive (limiting) flux, ϕ, through a standard background atmosphere consisting of O_2 and N_2 in the thermosphere, peak H density in the MLT $[H]_{peak}$, and exobase density $[H]_{exo}$. As shown by Waldrop and Paxton (2013), the modeled limb radiances are insensitive to variations in $[H]_{peak}$, and we adapt a constant value of 1.5×10^8 atoms/cm^3 for all inversions. The extension of H density above the exobase follows the analytical formulation by Bishop (1991), which uses the density $[H]_s$ and temperature T_s of an effective satellite population above the exobase as two additional free parameters that reflect the effect of $H-H^+$ charge exchange on exospheric structure. Necessary inputs, such as the densities of O, O_2 and N_2, and the height dependent ambient temperature T_n, are specified using the NRLMSISE-00 model (Picone et al., 2002).

The forward model calculates the H Ly_α emission radiance resulting from single and multiple scattering of solar Ly_α photons from a particular vantage along a specified LOS. The RT equations are solved using the numerical scheme developed by Anderson and Hord [1977], where the exosphere is discretized into 3-D spatial voxels and arranged in concentric spherical shells (zones). The evaluation of the transmission function is based on optical depth, which is in turn derived from the H density in a given discretized voxel. Within each zone, H density is assumed to vary exponentially along the radial dimension, rather than being constant as in the original LYAO-RT model formulation (Qin & Waldrop, 2016). The source function is evaluated using Gaussian quadrature along the path between photon scattering events. The optimal parameters describing an unknown H density profile are based on the best fit between forward model radiance profiles and measured GUVI radiance profiles, determined iteratively using the Gauss-Newton method. The inversion algorithm uses the relative, rather than absolute, Ly_α radiance across the limb as the data constraint and thus avoids systematic bias associated with uncertainty in the incident solar Ly_α flux at line center or the GUVI sensitivity (Waldrop & Paxton, 2013).

2.4. Jeans' Thermal Escape Flux

Jeans' classical theory of thermal evaporation is based on the assumptions that thermospheric H atoms are fully thermalized through frequent collisions and experience no collisions in the exosphere above the exobase (r_{exo}), which is defined as the height at which the H scale height equals the mean free path between collisions. A thermally evaporating H population is thus one whose radially outward speed at the exobase exceeds the gravitational escape velocity, v_{esc}, given by the following:

$$v_{esc} = \sqrt{2GM/r_{exo}} \tag{1}$$

where G is the gravitational constant of Earth and M is the mass of Earth.

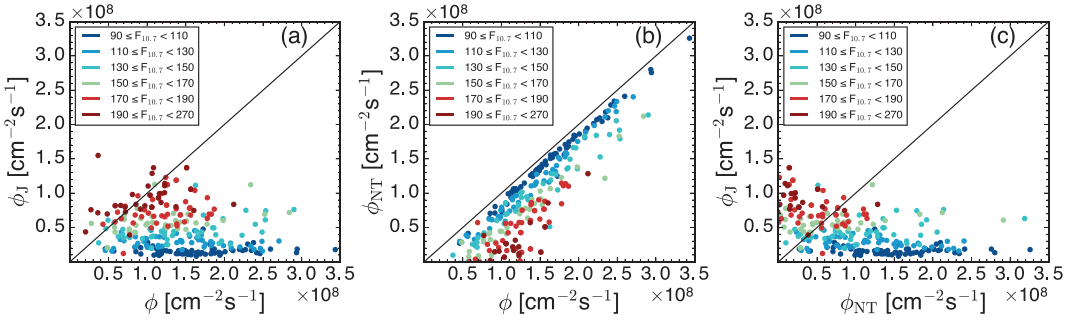

Figure 2. Comparison of the thermal Jeans' escape flux ϕ_J with the total vertical escape flux ϕ as a function of $F_{10.7}$ index (a), nonthermal escape flux ϕ_{NT} with the total vertical escape flux ϕ as a function of $F_{10.7}$ index (b), thermal Jeans' escape flux ϕ_J with the nonthermal escape flux ϕ_{NT} as a function of $F_{10.7}$ index (c). The total escape flux exceeds Jeans' escape flux at solar minimum, implying an increased contribution from nonthermal processes.

Jeans' escape flux, when derived as the integration of the high-energy tail of a symmetric Maxwellian H velocity distribution, simplifies as follows:

$$\phi_J = \frac{[H]_{exo}}{2}\sqrt{\frac{2k_B T_{exo}}{m\pi}}(1+\lambda_J)e^{-\lambda_J} \tag{2}$$

$$\lambda_J = \frac{E_{esc}}{k_B T_{exo}} = \frac{m v_{esc}^2}{2k_B T_{exo}} = \frac{GMm}{r_{exo} k_B T_{exo}} \tag{3}$$

where T_{exo} is the exobase temperature, m is the mass of atomic hydrogen, E_{esc} is the total escape energy, k_B is the Boltzmann constant, and λ_J is Jeans's escape parameter, defined as the ratio of gravitational potential energy GMm/r_{exo} to thermal energy $k_B T_{exo}$ (Chamberlain, 1963). It is important to account that the evaporative cooling caused by the high-energy escaping atoms can cause the H atom distribution to depart from the Maxwellian leading to potential overestimation of thermal flux using Jeans' expression (Brinkmann, 1971; Pierrard, 2003; Shizgal & Blackmore, 1986). In this work, we use the derived exobase density $[H]_{exo}$ and temperature T_{exo} at a nominal exobase altitude of 466 km, to calculate Jeans' thermal escape flux and investigate its solar activity variability.

3. Results

The results reported here are based on our analysis of GUVI Ly_α limb scans acquired from 2002–2007. For each scan, which is constructed as the average Ly_α radiance across the satellite track and within ±5° SZA bins near the solar ecliptic plane as described in Section 2.2, we derive the best fit parameters that govern the assumed functional form of the [H] distribution in altitude, [H](z). As described in Section 2.3, the forward RT model implements an unphysically discrete transition at a nominal exobase altitude separating the thermosphere (where the H density distribution is parameterized in terms of vertical diffusion) from the exosphere (where H density parameterization is based on effective satellite parameters). Derived H density distributions that exhibit unphysical discontinuities at the exobase are identified by their nonmonotonic decay across the transition and are not included in the analysis reported here. Out of a total of 638 scans considered in this analysis, this filter yields 320 independent [H] profiles and associated parameters H_{exo} and ϕ, which span all levels of solar activity, all seasons, and dayside local times from 6 to 18 hr local time (LT).

Estimates of H_{exo} are used in conjunction with T_{exo} specification by the NRLMSISE-00 model to derive the Jeans' escape flux ϕ_J according to equation (2). T_{exo} data associated with each individual limb scan that is used to construct one of the 320 average radiance profiles are similarly averaged within a given SZA bin. By interpreting the observed vertical flux ϕ in the thermosphere as the limiting escape flux (Shizgal & Arkos, 1996), we derive the nonthermal contributions to H escape as the difference $\phi_{NT} = \phi - \phi_J$ for each of the 320 measurements.

Figure 2 presents a direct comparison of the 320 estimates of ϕ, ϕ_J, and ϕ_{NT} as a function of solar activity using the solar $F_{10.7}$ index proxy. The solid line indicates equivalence between values plotted on the x

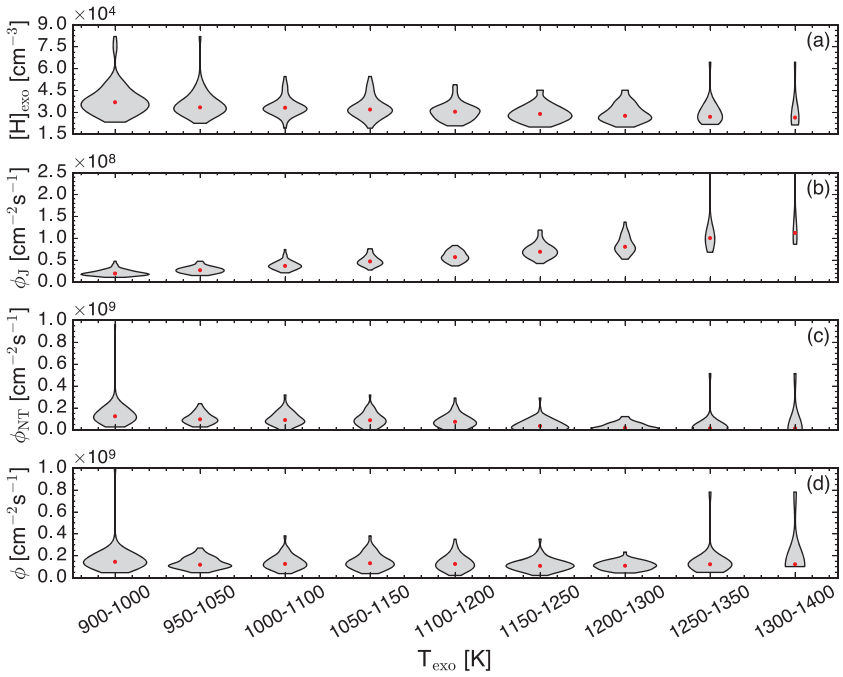

Figure 3. Variation of the exobase H density $[H]_{exo}$ (a), thermal Jeans' escape flux ϕ_J (b), nonthermal flux ϕ_{NT} (c), and total vertical flux ϕ (d) as a function of exospheric temperature T_{exo}. Each panel depicts "violin" plots which indicate the number of measurements, their distribution, and their dispersion within each T_{exo} bin. Median values of respective distributions are denoted by red dots. As T_{exo} increases, the exobase H density decreases, Jeans' flux increases, the nonthermal flux decreases whereas the total escape flux stays nearly constant.

and *y* axes in each panel. As seen in panel (a), the thermal evaporative Jeans' flux ϕ_J exhibits an increase with increasing solar activity and is typically smaller than the derived limiting flux ϕ for all solar activity levels (i.e., data are generally confined below the diagonal line of equivalence and the few exceptions are interpreted as unphysical measurement noise). Any deficit in ϕ_J relative to the total escape flux ϕ must be balanced by nonthermal escape, and the calculated ϕ_{NT} exhibits a corresponding dependence on solar activity as shown in panel (b). As with ϕ_J, ϕ_{NT} is smaller than the total escape flux ϕ throughout the solar activity (unphysical negative values associated with the rare cases of $\phi_J > \phi$ are not shown), with the largest deficits consistently observed at solar maximum. Panel (c) depicts the partitioning between ϕ_J and ϕ_{NT} as a means to assess their relative significance; in general, thermal escape is observed to dominate, by a factor of ~2, more often during solar maximum, while nonthermal processes tend to dominate by up to factors of ~5 or more during solar minimum.

The thermal flux, ϕ_J, is not inherently dependent on the $F_{10.7}$ index but rather exhibits its observed solar activity variation through its analytical dependence on T_{exo} (see equations (2) and (3)3), which is well known to increase with increasing solar activity (Picone et al., 2002). In order to further investigate this trend, we next examine the dependence of the derived density and flux parameters in terms of T_{exo}. Because the 320 independent estimates are not uniformly distributed with respect to their corresponding average T_{exo} value, we bin the parameters into 10 semi-overlapping temperature bins of 100 K spanning the entire range of average exospheric temperatures from 900–1400 K.

Figure 3 depicts the dependence of the derived density and flux parameters in terms of T_{exo}, in which the distribution of the data within each T_{exo} bin is depicted as a "violin" shape, where the width of the gray shaded region at a given value on the y axis (the parameter magnitude) corresponds to the number of observations having that value within that particular T_{exo} bin. The distributions in all T_{exo} bins are normalized to the maximum width among all bins, such that narrow distributions indicate that they are composed of fewer measurements relative to wider distributions. Inside each "violin" shape, a red dot indicates the median of the distribution. This data visualization concisely summarizes the skew, dispersion, and relative counting statistics of each distribution for ease in assessing the validity of observed climatological trends. As Figure 3 indicates, most derived density and flux parameters are slightly skewed toward larger values, suggestive of

Table 1
Statistical Estimates of ϕ, ϕ_J, and ϕ_{NT} [atoms cm^{-2} s^{-1}] as a Function of Exospheric Temperature (T_{exo})

T_{exo} [K]	ϕ ($\times 10^8$)	ϕ_J ($\times 10^8$)	ϕ_{NT} ($\times 10^8$)	ϕ_{NT}/ϕ
$900 < T_{exo} < 1000$	$1.42^{+0.92}_{-0.56}$	$0.20^{+0.07}_{-0.05}$	$1.17^{+0.97}_{-0.53}$	$0.83^{+0.10}_{-0.09}$
$950 < T_{exo} < 1050$	$1.21^{+0.61}_{-0.41}$	$0.26^{+0.08}_{-0.06}$	$0.92^{+0.62}_{-0.37}$	$0.75^{+0.11}_{-0.10}$
$1000 < T_{exo} < 1100$	$1.28^{+0.74}_{-0.47}$	$0.37^{+0.10}_{-0.08}$	$0.87^{+0.80}_{-0.42}$	$0.67^{+0.17}_{-0.14}$
$1050 < T_{exo} < 1150$	$1.31^{+0.82}_{-0.51}$	$0.47^{+0.11}_{-0.09}$	$0.79^{+0.86}_{-0.41}$	$0.59^{+0.19}_{-0.14}$
$1100 < T_{exo} < 1200$	$1.15^{+0.91}_{-0.51}$	$0.58^{+0.12}_{-0.10}$	$0.60^{+0.82}_{-0.39}$	$0.46^{+0.51}_{-0.24}$
$1150 < T_{exo} < 1250$	$1.03^{+0.69}_{-0.41}$	$0.70^{+0.17}_{-0.13}$	$0.32^{+0.90}_{-0.24}$	$0.27^{+0.50}_{-0.17}$
$1200 < T_{exo} < 1300$	$1.06^{+0.46}_{-0.32}$	$0.82^{+0.21}_{-0.16}$	$0.22^{+0.55}_{-0.16}$	$0.19^{+0.34}_{-0.12}$
$1250 < T_{exo} < 1350$	$1.22^{+0.71}_{-0.45}$	$1.01^{+0.30}_{-0.23}$	$0.24^{+0.56}_{-0.17}$	$0.17^{+0.27}_{-0.10}$
$1300 < T_{exo} < 1400$	$1.44^{+1.19}_{-0.65}$	$1.18^{+0.42}_{-0.31}$	$0.26^{+0.67}_{-0.19}$	$0.16^{+0.16}_{-0.08}$

an approximate lognormal distribution. For such distributions, the median (or equivalently, the geometric mean) represents the best estimate of the true value of $[H]_{exo}$ and is also robust to the effect of random errors and outliers (Joshi et al., 2018; Limpert et al., 2001).

As shown in Figure 3, the statistically significant increase in ϕ_J with increasing T_{exo}, which varies nearly linearly from 0.2×10^8 to 1.18×10^8 atoms cm^{-2} s^{-1} (panel b), occurs despite an associated but weaker decrease in derived estimates of $[H]_{exo}$ (panel a) from 4×10^4 atoms cm^{-3} at 950 K to 2×10^4 atoms cm^{-3} at 1350 K. Meanwhile, the limiting flux ϕ is observed to be nearly constant with varying temperature over the solar activity, at a value of $\sim 1.2 \times 10^8$ atoms cm^{-2} s^{-1} (panel d). As a result, the significant flux deficit $\phi_{NT} = \phi - \phi_J$, which we attribute as evidence for the existence of nonthermal escape mechanisms, exhibits the opposite temperature dependence of ϕ_J, decreasing from a median of 1.17×10^8 atoms cm^{-2} s^{-1} at 950 K to 0.26×10^8 atoms cm^{-2} s^{-1} at 1350 K. Table 1 summarizes the geometric mean and multiplicative standard deviations (Limpert et al., 2001) of the derived total, thermal, and nonthermal escape fluxes in each T_{exo} bin, along with the fractional contribution of nonthermal escape to the total inferred from the observed deficit in thermal evaporation. The statistical estimates represent the approximately lognormal flux distributions in the respective bins. As a result, the linear summation of thermal and nonthermal flux estimates is not expected to exactly match the total flux estimate. Our GUVI-based analysis suggests that nonthermal escape is minimally significant at solar maximum but becomes the dominant pathway for H escape for exobase temperatures below 1200 K, such that it accounts for more than 80% of the loss of H that is supplied to the exobase at solar minimum.

4. Discussion

4.1. Agreement With Prior Investigations of H Escape

The relatively insignificant dependence of the derived vertical flux of H through the thermosphere with varying T_{exo} confirms most previous results, which suggested that the escape of H is limited by its diffusion in all of its chemical forms through the MLT at a value that is nearly constant for exospheric temperatures above 800 K (Hunten, 1973; Hunten & Strobel, 1974; Liu & Donahue, 1974a, 1974b). The average value of $\phi = 1.2^{0.81}_{0.52} \times 10^8$ atoms $cm^{-2}s^{-1}$ resulting from our analysis is in good agreement with previous estimates of the diffusion-limited flux derived from semiempirical and physics-based photochemical modeling, which reported a value of $\phi = 1.5 \times 10^8$ atoms $cm^{-2}s^{-1}$ (Liu & Donahue, 1974a; Yung et al., 1989). On the other hand, we find that the total escape flux calculation of 3.5×10^8 atoms $cm^{-2}s^{-1}$ reported by Catling and Kasting (2017), and the value of 3.2×10^8 atoms $cm^{-2}s^{-1}$ reported by Yung et al. (1989) are significantly larger than the largest vertical diffusion flux derived from the GUVI data, which our statistical analysis suggests does not exceed 2.63×10^8 atoms $cm^{-2}s^{-1}$.

Our observations are also consistent with those obtained by the OGO-5 satellite (Bertaux, 1975). In that work, the thermal Jeans' escape flux was calculated using measured $[H]_{exo}$ (derived in turn from observations of H Ly_α emission), and nonthermal flux arising from charge exchange with H^+ ions was calculated approximately in terms of the exobase H density and its local scale height. Because the GUVI data used in

our analysis are restricted geographically to the ecliptic plane, such that potential nonthermal escape via the polar wind is not operative, the sum of thermal and nonthermal fluxes reported by Bertaux (1975) nominally corresponds to our reported estimate of total escape flux ϕ. As with our results, Bertaux (1975) observed the two escape components to exhibit opposite trends with respect to T_{exo}, such that their sum remained approximately constant at an average value of $\sim 1.4\times10^8$ atoms $cm^{-2}s^{-1}$, in good agreement with our results.

Although error bars on estimates of ϕ_J, ϕ_{NT}, or their sum were not reported in the Bertaux (1975) analysis, we note that the OGO-5-based estimates of total escape flux were reported to exhibit a weak local minimum at exobase temperatures near 1000 K, when contributions from thermal and nonthermal flux are approximately equal and relatively modest compared to their extreme values at solar maximum and minimum, respectively. At this temperature, the total (thermal + nonthermal) escape flux was estimated to be $\sim 1.3\times10^8$ atoms $cm^{-2}s^{-1}$, rising by ~15% to $\sim 1.5 \times 10^8$ atoms $cm^{-2}s^{-1}$ at the exobase temperature extremes of 900 and 1300 K considered (Bertaux, 1975). The GUVI-based limiting fluxes reported here also exhibit a similar dependence on exobase temperature, in that a local minimum in ϕ near 1100 K is ~25% smaller than the total escape flux at both the low and high temperature extremes, though we note that the large variance within each T_{exo}-binned distribution renders this trend statistically insignificant. On the other hand, the absolute range of ϕ values reported here are smaller, by ~20%, than those reported in either the Bertaux (1975) or Shizgal and Lindenfeld (1982) studies. The kinetic theory calculations of total (thermal + nonthermal) escape flux reported by Shizgal and Lindenfeld (1982), which were derived in an analysis similar to the Bertaux (1975) work, exhibited a monotonic increase with exobase temperature of ~11% from 1.52×10^8 atoms $cm^{-2}s^{-1}$ at 750 K to 1.69×10^8 atoms $cm^{-2}s^{-1}$ at 1250 K, a trend which GUVI does not support.

Our observed solar activity variability of thermal escape fluxes also agree reasonably well with these prior investigations, though significant discrepancies in their magnitude exist in this case as well. For a T_{exo} variation from 900–1400 K, our derived Jeans flux increases from 0.20×10^8 to 1.18×10^8 atoms $cm^{-2}s^{-1}$ and constitutes an increasing fraction of the total limiting flux that ranges from 17% to 84% with increasing temperature. This fractional contribution is higher than the increase from 9% to 50.3% with increasing T_{exo} reported by Liu and Donahue (1974a), while the magnitudes of the GUVI-based Jeans' fluxes are statistically significantly lower than those reported in that work, which range from 0.26×10^8 to 1.35×10^8 atoms $cm^{-2}s^{-1}$. Our ϕ_J values are also smaller than thermal escape fluxes derived by Shizgal and Lindenfeld (1982), which range from 0.16×10^8 cm^{-2} s^{-1} at $T_{exo} = 750$ K to 1.21×10^8 $cm^{-2}s^{-1}$ at 1250 K, though the increase in fractional contribution with increasing temperature, from ~10% to ~72%, is more consistent with our findings. The thermal escape fluxes derived from OGO-5 data, which range from $\sim 0.5 \times 10^8$ $cm^{-2}s^{-1}$ at 900 K to 1.4×10^8 $cm^{-2}s^{-1}$ at 1300 K, also exceed our GUVI-based estimations, both in terms of their absolute magnitude as well as their contribution to total escape at solar minimum, which was estimated to be as large as ~34% (Bertaux, 1975).

The discrepancies in both the limiting and thermal fluxes derived here relative to past results, which amount to their overestimation of total H escape by ~20%, may be attributed to the potential significance of eddy diffusion in reducing transport of H (in all of its chemical forms) out of the lower mesosphere. As described in detail by Colegrove et al. (1966) and Catling and Kasting (2017), the eddy diffusion coefficient scaled by the density gradients of H below the mesopause ($-k_{zz}\partial n/dz$), if accounted in the mesospheric H transport, serves to decrease the total diffusion-limited flux of H. However, most reported estimates of the limiting H flux through the mesopause have neglected the effect of eddy diffusion as well as temperature and density gradients of H in the mesosphere (Catling & Kasting, 2017; Liu & Donahue, 1974a). Such simplifications in the treatment of mesospheric H transport suggest a potential overestimation in the historical estimates of the limiting H flux. Updated estimates of k_{zz} (Qian et al., 2013; Salinas et al., 2016; Swenson et al., 2018), combined with the refinements in height-resolved measurements of MLT composition and temperature from TIMED/SABER (Mlynczak et al., 2018), provide all data-driven constraints necessary for such an assessment, though such analysis is beyond the scope of this work.

Because the nonthermal escape flux is derived here in terms of the deficit between the nearly constant limiting vertical flux and its temperature-dependent thermal escape component, we observe that the nonthermal fraction correspondingly increases with decreasing T_{exo}. This trend is highly consistent with previous observations that indicate opposite variation of nonthermal and Jeans' fluxes as a function of T_{exo} (Bertaux, 1975; Chamberlain, 1977; Hodges et al., 1981; Shizgal & Arkos, 1996; Shizgal & Lindenfeld, 1982). As T_{exo} increases from 900–1400 K, our derived ϕ_{NT} values decrease from 1.17×10^8 to 0.26×10^8 $cm^{-2}s^{-1}$,

a range which is significantly lower than the reported variation of 2.35×10^8 to 0.95×10^8 $cm^{-2}s^{-1}$ by Liu and Donahue (1974a) but in close agreement to the reported variation of 1.36×10^8 to 0.3×10^8 $cm^{-2}s^{-1}$ (Shizgal & Lindenfeld, 1982) and 1.07×10^8 to 0.47×10^8 $cm^{-2}s^{-1}$ (Bertaux, 1975). As noted above, because our analysis of GUVI data is restricted to midlatitudes, $H-H^+$ charge exchange should account for the entire nonthermal escape flux derived here. However, the T_{exo} dependence of our observed nonthermal flux differs from the T_{exo} dependence in the analytic expression of nonthermal escape flux induced by $H-H^+$ charge exchange that was adopted in the analyses by Bertaux (1975) and Shizgal and Lindenfeld (1982). This discrepancy may be attributed to the fact that the expression of Shizgal and Lindenfeld (1982) is based on an oversimplified collisional model of nonthermal escape, and our estimates of charge-exchange flux represent an independent constraint for a rigorous theoretical treatment of nonthermal escape in future studies. The kinetic theory governing such rigorous assessment of nonthermal escape, presented by Shizgal and Lindenfeld (1979) and Shizgal (1987), requires height-resolved measurements of exospheric temperature and density, differential cross sections of H and H^+, and nonequilibrium velocity distributions of H resulting from its interaction with ambient H^+ ions over a wide range of altitudes above and below the exobase. The inverse-theoretic estimation of H density using GUVI data, combined with velocity distributions derived from Monte Carlo simulations (Hodges, 1994) and/or solutions of the Boltzmann equation (Fahr & Shizgal, 1983), could provide the data-driven constraints to revisit such an investigation.

4.2. Sources of Potential Error

Our analysis of both the total escape flux and its partitioning into thermal and nonthermal pathways is predicated foremost on the accuracy of the RT model inversion using the GUVI observations of H Ly_α radiance across the Earth's limb. Specifically, the total limiting fluxes in the thermosphere are a direct product of the limb scan inversions, and the thermal flux calculations are linearly dependent on the inverted H density at the exobase. The forward RT model features several nonphysical assumptions which reduce the solution domain as a means of overcoming the lack of available data constraints on a potentially more sophisticated model formulation. First, the RT model assumes that the H density distribution is spherically symmetric and thus neglects potential asymmetries associated with solar radiation pressure, nonuniform satellite atom production, or polar depletion (Hodges, 1994). However, the reported analysis is restricted to midlatitude, dayside GUVI scans, which are dominated by photons scattered near the sunlit tangent heights of the viewing LOSs, where the column H density is largest. As a result, our limb scan analysis is relatively insensitive to such large-scale density variations, such that the derived parameters can be interpreted as accurately reflecting the local conditions near the thermospheric heights of the LOS tangent points.

The model also assumes a fixed location for the exobase altitude of 466 km, above which the H velocity distribution is assumed to be an isothermal Maxwellian defined by the exobase temperature specified by the NRLMSISE-00 model. While assumed temperatures are expected to well represent thermospheric conditions (Picone et al., 2002), such a formulation neglects the kinetic energization of H atoms through their charge exchange with hot H^+ ions, which our results suggest is a significant process even at solar maximum. While the RT model inclusion of satellite population parameters as described in Section 2.3 is intended to reflect the effect of such energization on the spatial distribution of H atoms above the exobase, the model's neglect of the associated enhancement in Doppler broadening of Ly_α photon scattering is a known, though practically unquantifiable, source of bias in the derived density distribution that most significantly affects H densities above the exobase, where nonthermal scattering effects are most pronounced. Because the results presented here rely on estimation of the thermospheric, rather than the exospheric, H density distribution, we assess the potential for error in the derived vertical fluxes and exobase densities to be relatively modest, particularly given the additional filtering of presumed unphysical solutions that we perform before analysis of our results (see Section 3).

The exobase height itself is also used to calculate Jeans' escape flux, and our assumption that it does not vary climatologically with exobase temperature is unphysical. However, Walker (1977) noted that the escape flux is only weakly sensitive to variations in exobase height. Based on Jeans' expression (equation (3)), Catling and Kasting (2017) have shown that the ratio of Jeans' flux at distinct exobase heights r_{exo} and r'_{exo} is proportional to the ratio of Jeans' parameter λ'_J and λ_J at the respective heights (i.e., $\frac{\phi'_J}{\phi_J} = \frac{1+\lambda'_J}{1+\lambda_J}$). Because λ_J is a slowly varying function of r_{exo}, we can write $\frac{\phi'_J}{\phi_J} = \frac{1+\lambda'_J}{1+\lambda_J} \approx 1$, which implies that Jeans' flux is insensitive to the exobase height used for its evaluation. As a result, the fixed exobase height used in our analysis should be considered reasonable and does not add any significant uncertainty to our results.

Our derivation of thermal escape flux is also predicated on the accuracy of the simple Jeans' expression used in the calculation. Jeans' classical theory assumes that the thermospheric H population is fully thermalized by binary collisions with the background gas during its vertical diffusion, that it reaches the exobase with a Maxwellian velocity distribution characteristic of the asymptotic exobase temperature and that the high-energy portion of the assumed symmetric Maxwellian tail escapes on collisionless trajectories. However, in a two or multicomponent atmosphere, previous studies suggested that the classical Jeans' expression can overestimate the terrestrial thermal escape flux of H by 20–30%, since it ignores the evaporative cooling caused by the loss of high-energy escaping atoms (Brinkmann, 1971; Pierrard, 2003; Shizgal & Blackmore, 1986). To account for this overestimation, several studies of terrestrial hydrogen escape introduce a corrective scaling factor for Jeans' approximation, typically ranging from 0.6–0.8 (Barakat & Lemaire, 1990; Bertaux, 1975; Brinkmann, 1970; Chamberlain & Smith, 1971), while kinetic investigations involving the solution of the Boltzmann equation have observed a wider variation in this correction factor, ranging from 0.3–0.8 (Fahr, 1976; Fahr & Shizgal, 1983; Hays & Liu, 1965; Shizgal & Blackmore, 1986; Shizgal & Lindenfeld, 1980).

Our neglect of this effect may lead to our overestimation of the thermal escape flux and consequent underestimation of the inferred nonthermal contribution to the total H escape. On the other hand, several other studies have also concluded that the classical Jeans' flux underestimates the true thermal evaporation, because the assumption that the H velocity distribution is a symmetric Maxwellian is inaccurate when nonthermal energization processes are operative. For a single-fluid hydrogen atmosphere, Merryfield and Shizgal (1994) solved the nonlinear Boltzmann equation and reported that the upward heat conduction due to escaping atoms from the tail of distribution creates enhanced escape of atoms above the exobase through occasional collisions. For a Jeans' parameter (λ_J) of 6.5, they found that Jeans' escape underestimated the actual thermal escape by ∼1.3. Volkov et al. (2011),Volkov et al. (2011) used a direct simulation Monte Carlo model to simulate the effect of angular anisotropy of the velocity distribution at the exobase, and found that for a Jeans' parameter (λ_J) ranging from 6–15, Jeans' escape underestimates the actual thermal escape at exobase by a factor ∼1.4–1.7. They suggested that the enhanced escape is caused by H atoms that gained escape velocities through collisions above the exobase. Similarly, Hodges et al. (1981) used a Monte Carlo model to simulate exospheric kinematics and observed anisotropic velocity distributions and temperature gradients in incoming-radial and transverse directions above the exobase, especially >1 R_E. They found that the Maxwellian distribution tail is replenished by collisions with nonthermal escaping atoms near the Earth's exobase only in the radially upward direction, but the nonisothermal and anisotropic velocity distribution of H atoms must be included in the RT treatment of Ly_α emission to account for the enhanced H escape in radial and transverse directions above the exobase. In addition to the Monte Carlo models, other models that approximate the moments of Boltzmann equation have similarly indicated the underestimation of thermal flux associated with the collisionless exosphere discontinuity inherent in Jeans' approximation (Lemaire et al., 2007). When Jeans' parameter is small (λ_J ∼1–7) but not sufficiently small for a hydrodynamic treatment of exosphere (λ_J <1), the effects of anisotropy and non-Maxwellian velocity distributions at and above the exobase become important. In our analysis, λ_J ≈5–8, but we neglect the effect of non-Maxwellian nonisotropic velocity distributions due to the absence of data or model-driven constraints on such velocity distributions. However, this potential bias should be considered in the interpretation of relative estimates of ϕ_J and ϕ_{NT} presented in Table 1. Future studies would benefit from considering the escape process as occurring from a range of altitudes instead of at a discrete exobase, as discussed in detail by Shizgal and Lindenfeld (1979) and Fahr and Shizgal (1983).

5. Conclusions

We present a rigorous quantification of terrestrial H escape, including estimates of the solar activity dependence of its partitioning into thermal and nonthermal components, based on analysis of optically thick H Ly_α radiances measured across Earth's midlatitude, dayside limb by TIMED/GUVI from 2002–2007. Our analysis yields the following general conclusions:

1. Total H escape appears to be diffusion limited at a rate of $\sim 1.2 \times 10^8$ atoms $cm^{-2}s^{-1}$ that exhibits no significant dependence on exobase temperature. This finding is consistent with prior investigations suggesting that the limiting flux is nearly constant over the solar activity. However, the average value reported here is smaller, by ∼20%, than previously reported estimates, which were derived from semiempirical

photochemical and kinetic theory modeling. This discrepancy may be due to the historical neglect of mesospheric eddy diffusion that serves to reduce the vertical flux of H supplied to the exobase.

2. The thermal flux calculated using Jeans' classical theory is consistently smaller than the observed diffusive flux of H through the thermosphere, which we interpret to be the upper limit on the total escape flux. This deficit implies that nonthermal escape processes represent a significant pathway for H escape relative to thermal evaporation under all levels of solar activity. Such nonthermal escape most likely arises from charge exchange with plasmaspheric H^+ ions, since high latitude GUVI data that might exhibit signatures of polar wind losses were excluded from our analysis.
3. Thermal escape is found to be most significant, comprising 84% of the total flux, at high exobase temperatures (~1400 K) corresponding to solar maximum conditions. Contributions from nonthermal escape increase with decreasing exobase temperature and constitute the overwhelmingly dominant component at solar minimum, reaching up to ~83% of the observed total flux of H supplied to the exobase for T_{exo} ~900 K. The solar activity dependence of the escape flux partitioning is in reasonable agreement with previous investigations, though, as with our estimates of total limiting flux, our estimates of absolute thermal fluxes are somewhat lower than prior investigations. This finding may be related to expected violations in the assumptions on which Jeans' expression for thermal flux is based.
4. The increase in Jeans' escape flux with increasing exobase temperature occurs despite a corresponding decrease in exobase density by a factor of ~2, from $\sim 4 \times 10^4$ atoms cm^{-3} at $T_{exo} = 950$ K to 2×10^4 atoms cm^{-3} at $T_{exo} = 1350$ K. Our observed variation in $[H]_{exo}$ is smaller in magnitude by a factor of ~2 than the corresponding variation by a factor of ~2.5, from $\sim 10 \times 10^4$ atoms cm^{-3} at $T_{exo} = 950$ K to $\sim 4 \times 10^4$ atoms cm^{-3} at $T_{exo} = 1350$ K, that is predicted by the semiempirical NRLMSISE-00 model (Picone et al., 2002).

While this work represents an unprecedented empirical quantification of H escape and its solar cycle variability, remaining uncertainties in our analysis regarding both the inverse-theoretic parameter estimation and the calculation of thermal flux partitioning warrant further investigation. Future analysis of TIMED/GUVI limb scans should explore the effect of kinetic energization on the velocity distribution of escaping H atoms, ideally guided by Monte Carlo simulations which accurately reflect the physics of both plasmaspheric charge exchange and polar wind. Additional constraints on RT model inversions using GUVI's observations of the Earth's disk would also benefit future investigations.

Acknowledgments
This work was supported by NASA Grant NNX16AF77G and NSF Grant 1733946. Yamuna Phal conducted the GUVI data processing and RT model inversion, while Pratik Joshi led the data analysis and manuscript preparation. Lara Waldrop supervised the project. The authors acknowledge Dr. Jianqi Qin for his contributions to the forward and inverse RT model development. The TIMED/GUVI limb scan data used in this study are publicly available and archived at the website (http://guvitimed.jhuapl.edu/). The data set of derived parameters related to this article can be found online (http://dx.doi.org/10.17632/js7bwkx9ry.1), an open-source online data repository by Elsevier hosted at Mendeley data. The authors thank the reviewers for their thorough examination and thoughtful suggestions.

References

Banks, P., & Kockarts, G. (1973). Chapter 16—The neutral exosphere. In P. Banks, & G. Kockarts (Eds.), *Aeronomy* (pp. 64–100). Academic Press. https://doi.org/10.1016/B978-0-12-077802-7.50008-7

Banks, P. M., & Holzer, T. E. (1968). The polar wind. *Journal of Geophysical Research*, *73*(21), 6846–6854. https://doi.org/10.1029/JA073i021p06846

Barakat, A. R., & Lemaire, J. (1990). Monte Carlo study of the escape of a minor species. *Physical Review A*, *42*(6), 3291–3302. https://doi.org/10.1103/PhysRevA.42.3291

Bertaux, J. L. (1975). Observed variations of the exospheric hydrogen density with the exospheric temperature. *Journal of Geophysical Research*, *80*(4), 639–642. https://doi.org/10.1029/JA080i004p00639

Bishop, J. (1991). Analytic exosphere models for geocoronal applications. *Planetary and Space Science*, *39*(6), 885–893. https://doi.org/10.1016/0032-0633(91)90093-P

Bishop, J. (2001). Thermospheric atomic hydrogen densities and fluxes from dayside Lyman α measurements. *Journal of Atmospheric and Solar-Terrestrial Physics*, *63*(4), 331–340. https://doi.org/10.1016/S1364-6826(00)00211-X

Brinkmann, R. T. (1970). Departures from jeans' escape rate for H and He in the Earth's atmosphere. *Planetary and Space Science*, *18*(4), 449–478. https://doi.org/10.1016/0032-0633(70)90124-8

Brinkmann, R. T. (1971). More comments on the validity of Jeans' escape rate. *Planetary and Space Science*, *19*(7), 791–794. https://doi.org/10.1016/0032-0633(71)90036-5

Carruthers, G. R., Page, T., & Meier, R. R. (1976). Apollo 16 Lyman alpha imagery of the hydrogen geocorona. *Journal of Geophysical Research*, *81*(10), 1664–1672. https://doi.org/10.1029/JA081i010p01664

Catling, D. C., & Kasting, J. F. (2017). *Atmospheric evolution on inhabited and lifeless worlds*. Cambridge University Press. https://doi.org/10.1017/9781139020558

Chamberlain, J. W. (1963). Planetary coronae and atmospheric evaporation. *Planetary and Space Science*, *11*(8), 901–960. https://doi.org/10.1016/0032-0633(63)90122-3

Chamberlain, J. W. (1977). Charge exchange in a planetary corona: Its effect on the distribution and escape of hydrogen. *Journal of Geophysical Research*, *82*(1), 1–9. https://doi.org/10.1029/JA082i001p00001

Chamberlain, J. W., & Smith, G. R. (1971). Comments on the rate of evaporation of a non-Maxwellian atmosphere. *Planetary and Space Science*, *19*(7), 675–684. https://doi.org/10.1016/0032-0633(71)90025-0

Christensen, A., Walterscheid, R., Ross, M., & Hays, P. (1994). *The global ultraviolet imager (GUVI) for the NASA TIMED mission*. SPIE-The International Society for Optical Engineering.

Cole, K. D. (1966). Theory of some quiet magnetospheric phenomena related to the geomagnetic tail. *Nature*, *211*(5056), 1385–1387.

Colegrove, F. D., Johnson, F. S., & Hanson, W. B. (1966). Atmospheric composition in the lower thermosphere. *Journal of Geophysical Research*, *71*(9), 2227–2236. https://doi.org/10.1029/JZ071i009p02227

Cucho-Padin, G., & Waldrop, L. (2018). Tomographic estimation of exospheric hydrogen density distributions. *Journal of Geophysical Research: Space Physics*, *123*, 5119–5139. https://doi.org/10.1029/2018JA025323

Fahr, H. (1976). Reduced hydrogen temperatures in the transition region between thermosphere and exosphere. *Annales de Geophysique*, *32*, 277–282.

Fahr, H. J., & Shizgal, B. (1983). Modern exospheric theories and their observational relevance. *Reviews of Geophysics*, *21*(1), 75–124. https://doi.org/10.1029/RG021i001p00075

Ganguli, S. B. (1996). The polar wind. *Reviews of Geophysics*, *34*(3), 311–348. https://doi.org/10.1029/96RG00497

Glocer, A., Gombosi, T. I., Toth, G., Hansen, K. C., Ridley, A. J., & Nagy, A. (2007). Polar wind outflow model: Saturn results. *Journal of Geophysical Research*, *112*, A01304. https://doi.org/10.1029/2006JA011755

Glocer, A., Kitamura, N., Toth, G., & Gombosi, T. (2012). Modeling solar zenith angle effects on the polar wind. *Journal of Geophysical Research*, *117*, A04318. https://doi.org/10.1029/2011JA017136

Glocer, A., Tóth, G., Gombosi, T., & Welling, D. (2009). Modeling ionospheric outflows and their impact on the magnetosphere, initial results. *Journal of Geophysical Research*, *114*, A05216. https://doi.org/10.1029/2009JA014053

Hays, P. B., & Liu, V. C. (1965). On the loss of gases from a planetary atmosphere. *Planetary and Space Science*, *13*(12), 1185–1212. https://doi.org/10.1016/0032-0633(65)90055-3

Hodges, R. R. (1994). Monte Carlo simulation of the terrestrial hydrogen exosphere. *Journal of Geophysical Research*, *99*(A12), 23,229–23,247. https://doi.org/10.1029/94JA02183

Hodges, R. R., Rohrbaugh, R. P., & Tinsley, B. A. (1981). The effect of the charge exchange source on the velocity and 'temperature' distributions and their anisotropies in the Earth's exosphere. *Journal of Geophysical Research*, *86*, 6917–6925. https://doi.org/10.1029/JA086iA08p06917

Hunten, D. M. (1973). The escape of light gases from planetary atmospheres. *Journal of the Atmospheric Sciences*, *30*(8), 1481–1494.

Hunten, D. M., & Strobel, D. F. (1974). Production and escape of terrestrial hydrogen. *Journal of the Atmospheric Sciences*, *31*(2), 305–317.

Jeans, J. (1923). The dynamical theory of gases. In *Cambridge Library Collection - Physical Sciences*, 4. Cambridge University Press. https://doi.org/10.1017/CBO9780511694370

Joshi, P. P., Waldrop, L. S., & Brum, C. G. M. (2018). Ionospheric O+ momentum balance through charge exchange with thermospheric O atoms. *Journal of Geophysical Research: Space Physics*, *123*, 9743–9761. https://doi.org/10.1029/2018JA025821

Kameda, S., Ikezawa, S., Sato, M., Kuwabara, M., Osada, N., Murakami, G., et al. (2017). Ecliptic north-south symmetry of hydrogen geocorona. *Geophysical Research Letters*, *44*, 11,706–711,712. https://doi.org/10.1002/2017GL075915

Krall, J., Glocer, A., Fok, M.-C., Nossal, S. M., & Huba, J. D. (2018). The unknown hydrogen exosphere: Space weather implications. *Space Weather*, *16*, 205–215. https://doi.org/10.1002/2017SW001780

Lemaire, J. F., Peterson, W. K., Chang, T., Schunk, R. W., Barakat, A. R., Demars, H. G., & Khazanov, G. V. (2007). History of kinetic polar wind models and early observations. *Journal of Atmospheric and Solar-Terrestrial Physics*, *69*(16), 1901–1935. https://doi.org/10.1016/j.jastp.2007.08.011

Limpert, E., Stahel, W. A., & Abbt, M. (2001). Log-normal Distributions across the Sciences: Keys and Clues On the charms of statistics, and how mechanical models resembling gambling machines offer a link to a handy way to characterize log-normal distributions, which can provide deeper insight into va. *Bioscience*, *51*(5), 341–352.

Liu, S., & Donahue, T. (1974a). Mesospheric hydrogen related to exospheric escape mechanisms. *Journal of the Atmospheric Sciences*, *31*(5), 1466–1470.

Liu, S., & Donahue, T. (1974b). Realistic model of hydrogen constituents in the lower atmosphere and escape flux from the upper atmosphere. *Journal of the Atmospheric Sciences*, *31*(8), 2238–2242.

Liu, S., & Donahue, T. (1974c). The aeronomy of hydrogen in the atmosphere of the Earth. *Journal of the Atmospheric Sciences*, *31*(4), 1118–1136.

Merryfield, W. J., & Shizgal, B. D. (1994). Discrete velocity model for an escaping single-component atmosphere. *Planetary and Space Science*, *42*(5), 409–419. https://doi.org/10.1016/0032-0633(94)90130-9

Mlynczak, M. G., Hunt, L. A., Russell, J. M. III, & Marshall, B. T. (2018). Updated SABER night atomic oxygen and implications for SABER ozone and atomic hydrogen. *Geophysical Research Letters*, *45*(11), 5735–5741. https://doi.org/10.1029/2018GL077377

Paxton, L. J., A. B. Christensen, D. C. Humm, B. S. Ogorzalek, C. T. Pardoe, D. Morrison, et al.nd et al. (1999), Global ultraviolet imager (GUVI): Measuring composition and energy inputs for the NASA Thermosphere Ionosphere Mesosphere Energetics and Dynamics (TIMED) mission.

Picone, J. M., Hedin, A. E., Drob, D. P., & Aikin, A. C. (2002). NRLMSISE-00 empirical model of the atmosphere: Statistical comparisons and scientific issues. *Journal of Geophysical Research*, *107*(A12), SIA 15–1–SIA 15–16. https://doi.org/10.1029/2002JA009430

Pierrard, V. (2003). Evaporation of hydrogen and helium atoms from the atmospheres of Earth and Mars. *Planetary and Space Science*, *51*(4), 319–327. https://doi.org/10.1016/S0032-0633(03)00014-X

Qian, L., Burns, A. G., Solomon, S. C., & Wang, W. (2013). Annual/semiannual variation of the ionosphere. *Geophysical Research Letters*, *40*, 1928–1933. https://doi.org/10.1002/grl.50448

Qian, L., Solomon, S. C., & Kane, T. J. (2009). Seasonal variation of thermospheric density and composition. *Journal of Geophysical Research*, *114*, A01312. https://doi.org/10.1029/2008JA013643

Qin, J., & Waldrop, L. (2016). Non-thermal hydrogen atoms in the terrestrial upper thermosphere. *Nature Communications*, *7*, 13655. https://doi.org/10.1038/ncomms13655

Salinas, C. C. J. H., Chang, L. C., Liang, M.-C., Yue, J., Russell, J. III, & Mlynczak, M. (2016). Impacts of SABER CO_2-based eddy diffusion coefficients in the lower thermosphere on the ionosphere/thermosphere. *Journal of Geophysical Research: Space Physics*, *121*, 1212–8092. https://doi.org/10.1002/2016JA023161

Shizgal, B. (1987). Hot hydrogen and deuterium in the exosphere of Venus. *Advances in Space Research*, *7*(12), 73–77. https://doi.org/10.1016/0273-1177(87)90203-1

Shizgal, B., & Blackmore, R. (1986). A collisional kinetic theory of a plane parallel evaporating planetary atmosphere. *Planetary and Space Science*, *34*(3), 279–291. https://doi.org/10.1016/0032-0633(86)90133-9

Shizgal, B., & Lindenfeld, M. J. (1979). Energy distribution function of translationally hot O(3P) atoms in the atmosphere of Earth. *Planetary and Space Science*, *27*(11), 1321–1332. https://doi.org/10.1016/0032-0633(79)90055-2

Shizgal, B., & Lindenfeld, M. J. (1980). Further studies of non-maxwellian effects associated with the thermal escape of a planetary atmosphere. *Planetary and Space Science*, *28*(2), 159–163. https://doi.org/10.1016/0032-0633(80)90091-4

Shizgal, B., & Lindenfeld, M. J. (1982). A simple kinetic theory calculation of terrestrial atomic hydrogen escape fluxes induced by charge exchange collisions. *Journal of Geophysical Research*, *87*(A2), 853–858. https://doi.org/10.1029/JA087iA02p00853

Shizgal, B. D., & Arkos, G. G. (1996). Nonthermal escape of the atmospheres of Venus, Earth, and Mars. *Reviews of Geophysics*, *34*(4), 483–505. https://doi.org/10.1029/96RG02213

Swenson, G., Yee, Y., Vargas, F., & Liu, A. (2018). Vertical diffusion transport of atomic oxygen in the mesopause region consistent with chemical losses and continuity: Global mean and inter-annual variability. *Journal of Atmospheric and Solar-Terrestrial Physics*, *178*, 47–57. https://doi.org/10.1016/j.jastp.2018.05.014

Thomas, G. E., & Vidal-Madjar, A. (1978). Latitude variations of exospheric hydrogen and the polar wind. *Planetary and Space Science*, *26*(9), 873–882. https://doi.org/10.1016/0032-0633(78)90110-1

Tinsley, B. (1973). The diurnal variation of atomic hydrogen. *Planetary and Space Science*, *21*, 686.

Tinsley, B. A., Hodges, R. R. Jr., & Strobel, D. F. (1975). Diurnal variations of atomic hydrogen: Observations and calculations. *Journal of Geophysical Research (1896-1977)*, *80*(4), 626–634. https://doi.org/10.1029/JA080i004p00626

Vidal-Madjar, A., & Bertaux, J. L. (1972). A calculated hydrogen distribution in the exosphere. *Planetary and Space Science*, *20*(8), 1147–1162. https://doi.org/10.1016/0032-0633(72)90004-9

Vidal-Madjar, A., & Thomas, G. E. (1978). The terrestrial hydrogen problem. *Planetary and Space Science*, *26*(9), 863–871. https://doi.org/10.1016/0032-0633(78)90109-5

Volkov, A. N., Johnson, R. E., Tucker, O. J., & Erwin, J. T. (2011). Thermally driven atmospheric escape: Transition from hydrodynamic to Jeans escape. *The Astrophysical Journal*, *729*(2), L24. https://doi.org/10.1088/2041-8205/729/2/l24

Volkov, A. N., Tucker, O. J., Erwin, J. T., & Johnson, R. E. (2011). Kinetic simulations of thermal escape from a single component atmosphere. *Physics of Fluids*, *23*(6), 66,601. https://doi.org/10.1063/1.3592253

Waldrop, L., & Paxton, L. J. (2013). Lyman α airglow emission: Implications for atomic hydrogen geocorona variability with solar cycle. *Journal of Geophysical Research: Space Physics*, *118*, 5874–5890. https://doi.org/10.1002/jgra.50496

Walker, J. C. G. (1977). *Evolution of the atmosphere/James C. G. Walker, xiii*, (p. 318). New York: Macmillan.

Yung, Y. L., Wen, J.-S., Moses, J. I., Landry, B. M., Allen, M., & Hsu, K.-J. (1989). Hydrogen and deuterium loss from the terrestrial atmosphere: A quantitative assessment of nonthermal escape fluxes. *Journal of Geophysical Research*, *94*(D12), 14,971–14,989. https://doi.org/10.1029/JD094iD12p14971